Multi-frequency SuperDARN interferometer calibration

E. G. Thomas[1] **and S. G. Shepherd**[1]

[1]Dartmouth College, Hanover, NH, USA

Key Points:

- Calibration of SuperDARN interferometer angle of arrival data remains an outstanding challenge
- Analysis of data at multiple frequencies can overcome the inherent 2π measurement ambiguity in the phase correction factor (t_{diff})
- Example applications are shown for historical and contemporary multi-frequency SuperDARN observations

Corresponding author: Evan G. Thomas, `evan.g.thomas@dartmouth.edu`

Abstract

The ground-based, high-frequency radars of the Super Dual Auroral Radar Network (SuperDARN) observe backscatter from ionospheric field-aligned plasma irregularities and features on the Earth's surface out to ranges of several thousand kilometers via over-the-horizon propagation of transmitted radio waves. Interferometric techniques can be applied to the received signals at the primary and secondary antenna arrays to measure the vertical angle of arrival, or elevation angle, for more accurate geolocation of SuperDARN observations. Calibration of SuperDARN interferometer measurements however remains challenging for several reasons, including a 2π ambiguity in the phase correction factor needed to account for differences in the electrical path lengths between signals received at the two antenna arrays. We present a new technique using multi-frequency ionospheric and ground backscatter observations for the calibration of SuperDARN interferometer data, and demonstrate its application to both historical and recent data.

1 Introduction

The Super Dual Auroral Radar Network (SuperDARN) is an international collaboration of ground-based, high-frequency (HF) radars which monitors space weather conditions in the Earth's ionosphere and lower atmosphere (Greenwald et al., 1995; Chisham et al., 2007; Nishitani et al., 2019). Most SuperDARN radars have a smaller interferometer antenna array, displaced from the main antenna array by ∼60–185 m, to measure the vertical angle of arrival, or elevation angle, of the received radar signals (Shepherd, 2017). These elevation angle measurements are important for the accurate geolocation of SuperDARN backscatter observations, both from field-aligned ionospheric irregularities for mapping two-dimensional plasma flow (e.g., Ruohoniemi & Baker, 1998; Bristow et al., 2022) and from the Earth's land and sea surfaces (Greenwald et al., 2017).

In SuperDARN radar systems, the physical separation between the main and interferometer antenna arrays introduces a phase delay in the signals that are received by each antenna that depends on the elevation angle. In addition, there are typically differences in the electrical path lengths from the two antenna arrays to the point at which the return signals are correlated. The corresponding difference in the signal travel time along each path, known as t_{diff}, causes a systematic offset in the measured phase difference between the signals from the two arrays, which must be accounted for (Chisham et al., 2021).

While it is possible to measure these electrical path differences, it can be challenging without specialized test equipment and cannot be performed for historical datasets. Several methods have therefore been developed to estimate t_{diff} using ionospheric scatter (IS) or ground scatter (GS) measurements assumed to follow known propagation characteristics, e.g., from meteor trails (Chisham & Freeman, 2013; Chisham, 2018), $\frac{1}{2}$-hop E-region IS (Ponomarenko et al., 2018), 1-hop F-region GS (Ponomarenko et al., 2015), or targets with a known ground location such as artificially generated irregularities (Burrell et al., 2016). However, because SuperDARN radars typically operate at only one or two frequencies, these techniques are susceptible to a 2π ambiguity when estimating t_{diff} and therefore may not identify the true value which is valid across all possible operating frequencies (assuming one exists).

To address this issue, we have extended the "virtual height method" described by Chisham et al. (2021) to utilize multi-frequency observations of both IS and GS echoes for the automated calibration of t_{diff}. The methodology of this multi-frequency approach is described in section 2. In sections 3 and 4 we demonstrate the application of this technique to historical SuperDARN data, as well provide contemporary t_{diff} estimates for selected radars. In section 5 we discuss our results from applying the technique.

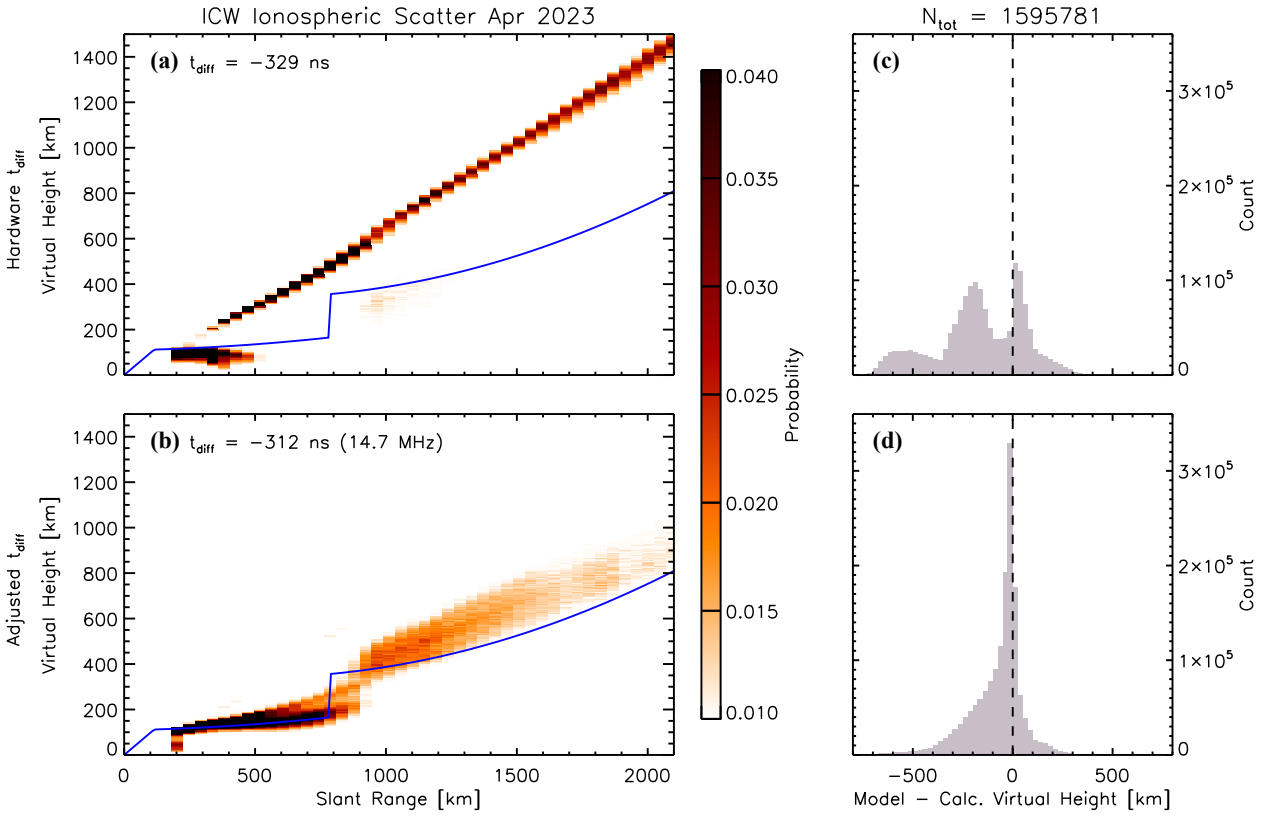

Figure 1. Virtual height comparison method for the Iceland West (ICW) SuperDARN radar when using the initial t_{diff} estimate (-329 ns) and the t_{diff} found by adjusting the $\frac{1}{2}$-hop ionospheric backscatter to match the Chisham VHM (-312 ns at 14.7 MHz), after Chisham et al. (2021). Panels (a) and (b) show two-dimensional histograms of the slant range and virtual height distribution of the ICW data from the entire month of April 2023 for ranges 0–2100 km, with the Chisham VHM overlaid in blue. Panels (c) and (d) show histograms of the difference between the modeled and measured virtual heights at these same ranges.

2 Methodology

The virtual height comparison method introduced by Chisham et al. (2021) is based on the presumption that, for a correct t_{diff} value, the observed elevation angle (or virtual height) variations with range should nominally match the behavior of an empirical virtual height model (VHM). These VHMs are the default method for geolocation of line-of-sight (LOS) SuperDARN observations and are required for use at radar sites which either do not have an interferometer antenna array or t_{diff} has not yet been calibrated (e.g., Chisham et al., 2008; Thomas & Shepherd, 2022). Chisham et al. (2021) demonstrated how, for $\frac{1}{2}$-hop IS, an obviously incorrect t_{diff} value can be adjusted until the observed distribution of slant range and virtual height align with the VHM of Chisham et al. (2008) (hereafter referred to as the Chisham VHM).

As an example, we apply this virtual height calibration technique to the recently constructed Iceland West (ICW) SuperDARN radar which, along with the co-located Iceland East radar, saw first light in January 2023. An initial t_{diff} estimate of -329 ns was determined for ICW based on the difference in coaxial cable lengths from the main and interferometer antenna arrays to a central equipment shelter housing the radar electronics. Figure 1a shows the joint probability distribution of IS observed by ICW during the

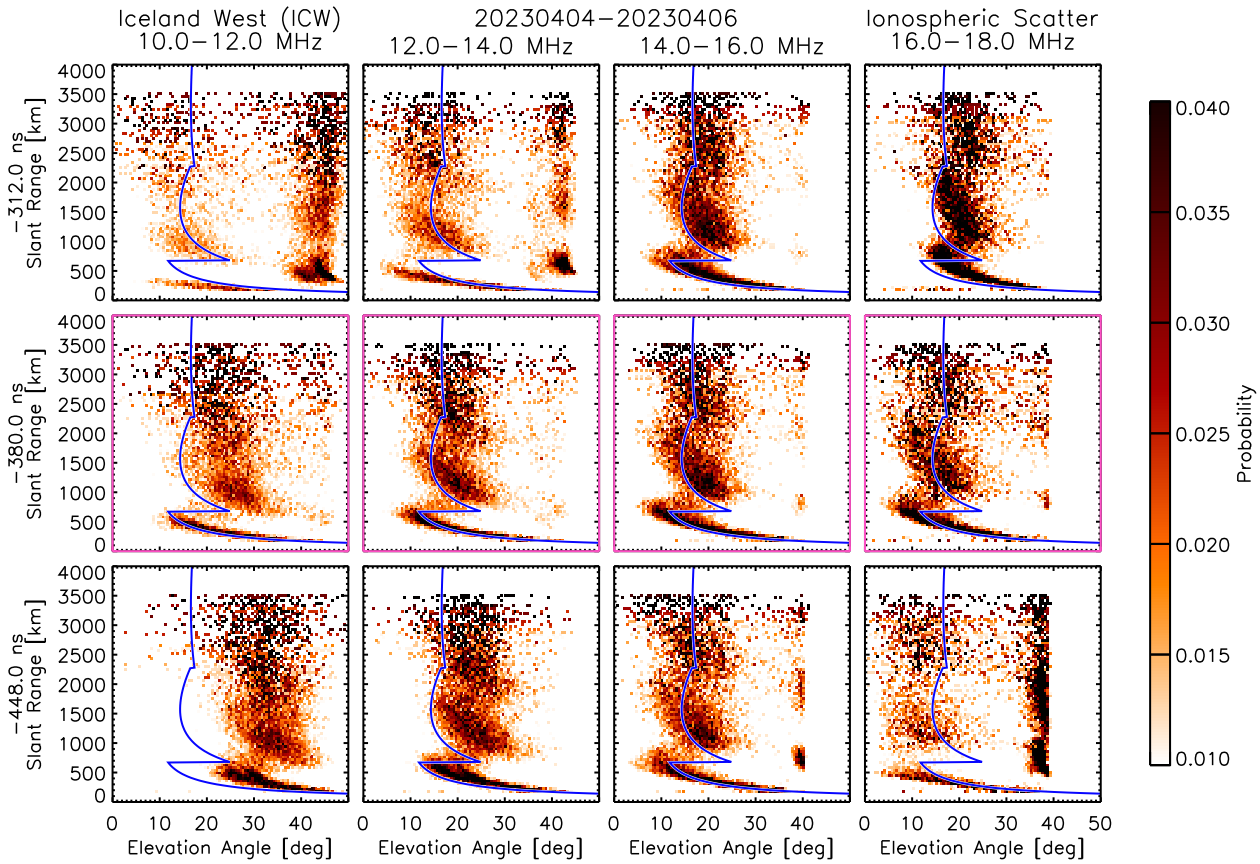

Figure 2. Joint probability distributions of elevation angle and slant range for ionospheric scatter observed by ICW on 4–6 April 2023 in 0.5° elevation and 45 km range bins, sorted by radar operating frequency into four bands between 10 MHz (left column) and 18 MHz (right column) and calculated using three values of t_{diff}: −312 ns (top row), −380 ns (middle), and −448 ns (bottom). The Chisham et al. (2008) empirical virtual height model is overlaid on each panel in blue.

entire month of April 2023 at a single frequency (14.7 MHz) divided into 45 km range and 5 km height bins, with the Chisham VHM overlaid in blue. Note the distributions are normalized by the maximum occurrence at each range bin, after Chisham et al. (2008, 2021).

Beyond ∼500 km range, all of the data in Figure 1a are aliased to very large and linearly increasing virtual heights, suggesting the initial t_{diff} estimate is incorrect. The histogram in Figure 1c shows that the distribution of differences between the VHM and calculated virtual heights has multiple peaks: the peak near zero is likely due to the near-range E-region echoes where the virtual heights are small, while the other two peaks at larger negative values are likely attributable to the $\frac{1}{2}$-hop F-region echoes at farther ranges where the calculated virtual heights are much greater than the model suggests. Figure 1b shows the same data using a revised t_{diff} value of −312 ns where the calculated virtual heights now align much more closely with the Chisham VHM predictions in both the $\frac{1}{2}$-hop E- and F-region regimes. The corresponding histogram in Figure 1d confirms this improved agreement with a single-peaked distribution located maximizing near zero and a tail towards negative values. This tail can again be attributed to $\frac{1}{2}$-hop F-region echoes with slightly greater virtual heights than the empirical Chisham VHM predicts.

In Figure 2 we consider multi-frequency data observed by ICW with a special sounding mode over three days in April 2023, with each of the four columns corresponding to a 2 MHz frequency band between 10–18 MHz. Note the ICW radar was actually operating at 8 equally-spaced frequencies from 9.6–16.6 MHz at 1 MHz increments; more details about this special sounding mode are provided in section 4. Each panel in Figure 2 shows joint probability distributions of the observed IS divided into 0.5° elevation and 45 km range bins. A different t_{diff} value is used in each row to calculate the elevation angles: −312, −380, and −448 ns. Note that −312 ns (top row) was the value previously identified with the virtual height comparison method in Figure 1. Overlaid on all of the panels in blue is the Chisham VHM; horizontal segments indicate transitions between the three propagation modes described by this model (i.e., $\frac{1}{2}$-hop E-region, $\frac{1}{2}$-hop F-region, and $1\frac{1}{2}$-hop F-region backscatter).

In the third column of Figure 2 (14–16 MHz) the elevation-range distributions appear nearly identical regardless of which of the three t_{diff} values are used. Specifically, the near-range echoes in all three panels closely follow the empirical VHM curve corresponding to $\frac{1}{2}$-hop backscatter from either meteor trails or E-region irregularities. However for the other frequency bands, the elevation-range distributions in each of the three rows no longer agree with one another. Only when calculating elevation angles using the t_{diff} value from the center row (−380 ns, pink outline) do the distributions behave similarly at each frequency band while also nominally aligning with the Chisham VHM. Note the t_{diff} values applied to each row of Figure 2 are a multiple of 68 ns, or one wavelength at 14.7 MHz (i.e., near the center of the 2 MHz frequency band in the third column), to illustrate the 2π ambiguity when estimating t_{diff}.

While this tuning procedure may be performed manually to find the optimal t_{diff} value for all frequency bands, in practice an automated procedure is desirable given the large dataset from the more than 30 continuously operating SuperDARN radars. Here we describe a simple iterative procedure which has been found to quickly converge to an appropriate t_{diff}, examples of which are shown in the following sections:

1. For each frequency bin, calculate elevation angles observed by a given radar using the generalized algorithm of Shepherd (2017) for $-1000 < t_{\text{diff}} < +1000$ ns, at steps of 5 ns
2. Find the median difference between an empirical VHM and the calculated elevation angles for each t_{diff} at each frequency
3. Identify the t_{diff} for which the median elevation angle difference is a minimum across all frequency bins
4. Repeat steps 1–3 using a new search range of ±10 ns centered about the previously identified t_{diff} value, at steps of 1 ns

Note there are currently three available SuperDARN VHMs: the "standard" VHM, the Chisham VHM, and the Christmas Valley VHM (hereafter referred to as the CV VHM). Both the standard and Chisham VHMs are restricted to IS only, while the CV VHM has separate models for IS and GS propagation modes (Thomas & Shepherd, 2022). In the next sections we use the CV VHM rather than the Chisham VHM to allow inclusion of both IS and GS observations in our analysis.

3 Common Mode Data

To our knowledge, the earliest available multi-frequency SuperDARN observations with quality interferometer data were collected by the Goose Bay radar (GBR) during standard operations from Jan–Mar 1994 on four frequency bands: 11.5–12.0 MHz, 12.3–13.0 MHz, 14.4–14.9 MHz, and 16.4–16.9 MHz. Figure 3 shows joint probability distributions of (top) IS and (bottom) GS observations by GBR during this 3-month inter-

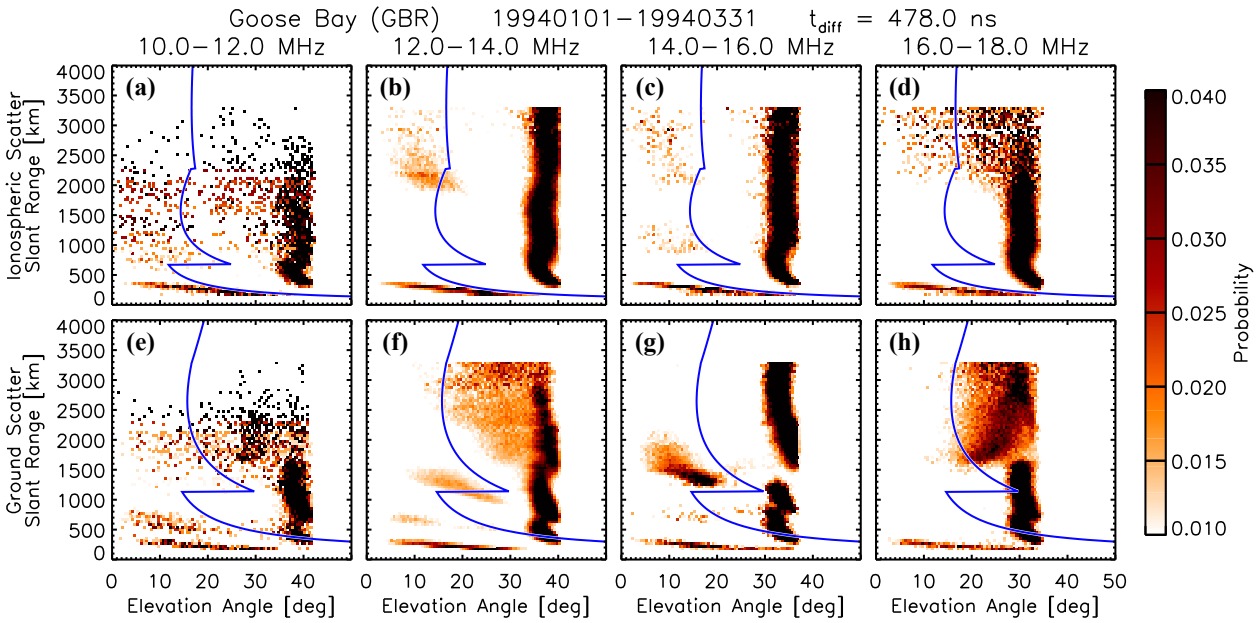

Figure 3. Joint probability distributions of elevation angle and slant range for (top) ionospheric scatter and (bottom) ground scatter observed by the Goose Bay (GBR) SuperDARN radar from Jan–Mar 1994 in 0.5° elevation and 45 km range bins, sorted by radar operating frequency into four bands between 10–18 MHz, using the current hardware t_{diff} value of 478 ns. The Christmas Valley empirical virtual height model is overlaid on each panel in blue (Thomas & Shepherd, 2022).

val divided into 0.5° elevation and 45 km range bins and normalized in the same fashion as Figure 2. Each column corresponds to a different frequency band, and the empirical CV VHM is overlaid on each panel in blue for reference.

The elevation angles in Figure 3 are calculated using the t_{diff} value of 487 ns listed for GBR in the SuperDARN analysis software for these dates (SuperDARN Data Analysis Working Group et al., 2022). While observations from a high-latitude radar such as GBR are not expected to perfectly align with the empirical CV VHM (which was derived from mid-latitude observations), the data and model curves do not agree for any of the four frequency bands. In fact, all but the nearest range data are aliased to very high elevation angles, which Chisham et al. (2021) demonstrated to be a likely symptom of an incorrect t_{diff} value (e.g., Figure 1a).

Applying the multi-frequency calibration technique suggests a t_{diff} value of 457 ns, the result of which can be seen in Figure 4. Here we see the IS and GS measurements are now much better aligned with the empirical CV VHM at all four frequency bands, with a few notable exceptions. The GS distributions in both the 10–12 MHz (Figure 4e) and 16–18 MHz (Figure 4h) bands appear "mirrored" for ranges beyond 1500 km and elevation angles above 20°. These regions are likely associated with observations from the backlobe, which is a well-known characteristic of the log-periodic antenna design used by the GBR radar (e.g., Milan et al., 1997; André et al., 1998).

4 Sounding Mode Data

Hughes et al. (2002) developed a special sounding mode for SuperDARN radars which utilized the ∼12 s of down-time available at the end of each standard 1 min az-

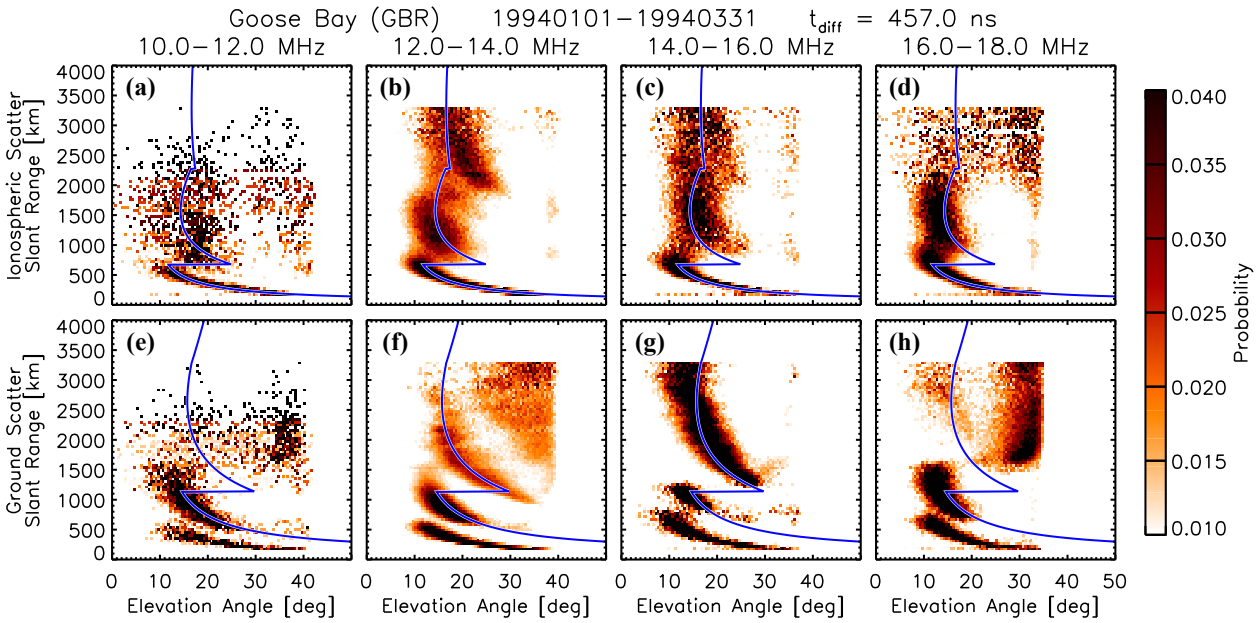

Figure 4. Joint probability distributions of elevation angle and slant range for (a-d) ionospheric scatter and (e-h) ground scatter observed by GBR in the same format as Figure 3, using a revised t_{diff} value of 457 ns.

imuthal scan to step through a range of ∼8 equally-spaced frequencies in the 8–20 MHz band. A complete scan across all radar beams and sounding frequencies can be obtained every ∼15–30 min with this mode, and is therefore an ideal candidate for the multi-frequency calibration approach. Unfortunately, there are several challenges associated with the original sounding mode data files, including their minimally documented binary format and limited distribution. Furthermore, the elevation angles stored in the sounding data files were calculated using on-site processing software at the radars, seemingly preventing any calibration using post-processing techniques (e.g., Chisham et al., 2021).

Nevertheless, sounding mode files from a subset of radars have been recovered for various times over the years 2005–2018. By making an educated assumption about the original t_{diff} and interferometer offset values applied by the on-site FITACF software, one can convert the recorded elevation angles back to the observed phase differences (ψ_{obs}) such that post-processing calibration techniques can be applied in pursuit of a different t_{diff}. Using the notation of Shepherd (2017), this conversion takes the form

$$\psi_{obs} = 2\pi f_{\text{TX}} \left[\frac{Y}{c} (\cos^2 \phi_0 - \sin^2 \alpha)^{\frac{1}{2}} - t_{\text{diff}} \right] \quad (1)$$

where f_{TX} is the radar operating frequency, c is the speed of light in free space, Y is the geometric separation between the main and interferometer antenna arrays along the array normal direction (with $+Y$ in the direction of the array normal), α is the elevation angle, and ϕ_0 is the direction at $\alpha = 0°$ (horizontal) set electronically by the radar hardware. This expression is equivalent to the original elevation angle equation (e.g., Milan et al., 1997; André et al., 1998) which did not account for interferometer offsets in the X- or Z-directions.

Another radar we applied this technique to is TIGER Bruny (TIG) which operated the sounding mode periodically from 2005–2011. Figure 5 shows joint probability distributions of elevation angle and slant range for GS echoes observed by TIG for the entire month of Dec 2005 as extracted from the sounding mode files. Each of the nine

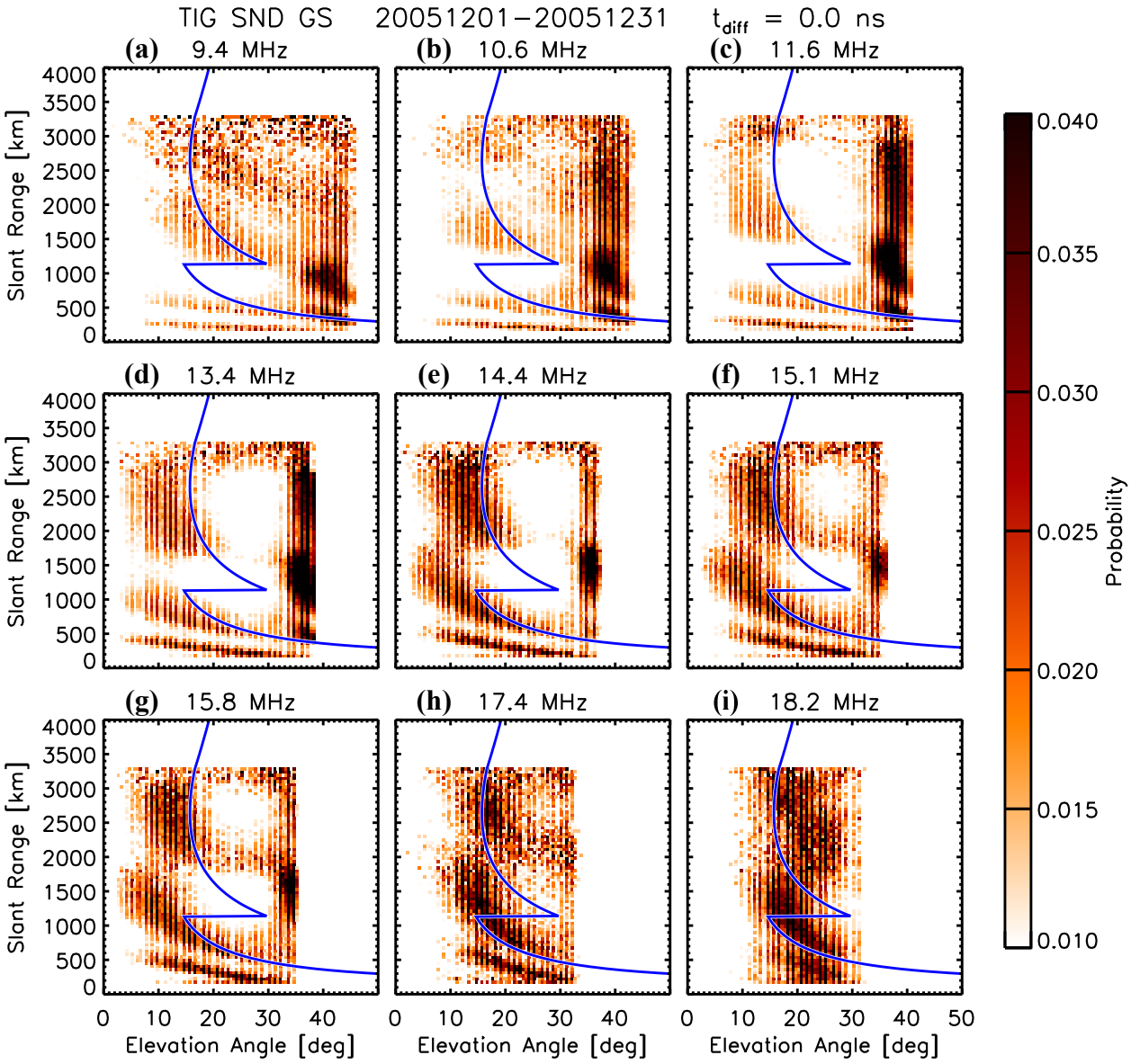

Figure 5. Joint probability distributions of elevation angle and slant range for ground scatter observed by the TIGER Bruny (TIG) radar during the entire month of Dec 2005 at 9 sounding mode frequencies, using the current hardware t_{diff} value of 0 ns. The Christmas Valley ground scatter virtual height model is overlaid on each panel in blue (Thomas & Shepherd, 2022). Note the vertical striping is due to the integer precision of the original sounding mode data format (Hughes et al., 2002).

panels corresponds to a different sounding frequency, and the GS component of the CV VHM is again overlaid in blue for reference. Based on current and historical versions of the TIG information in the SuperDARN analysis software, we have assumed a t_{diff} value of 0 ns and an interferometer offset solely in the Y-direction of 100 m were used in the original on-site calculation of these elevation angles. Note the vertical striping in Figure 5 is due to the integer precision of the elevation angles (and all other parameters) stored in the sounding mode files.

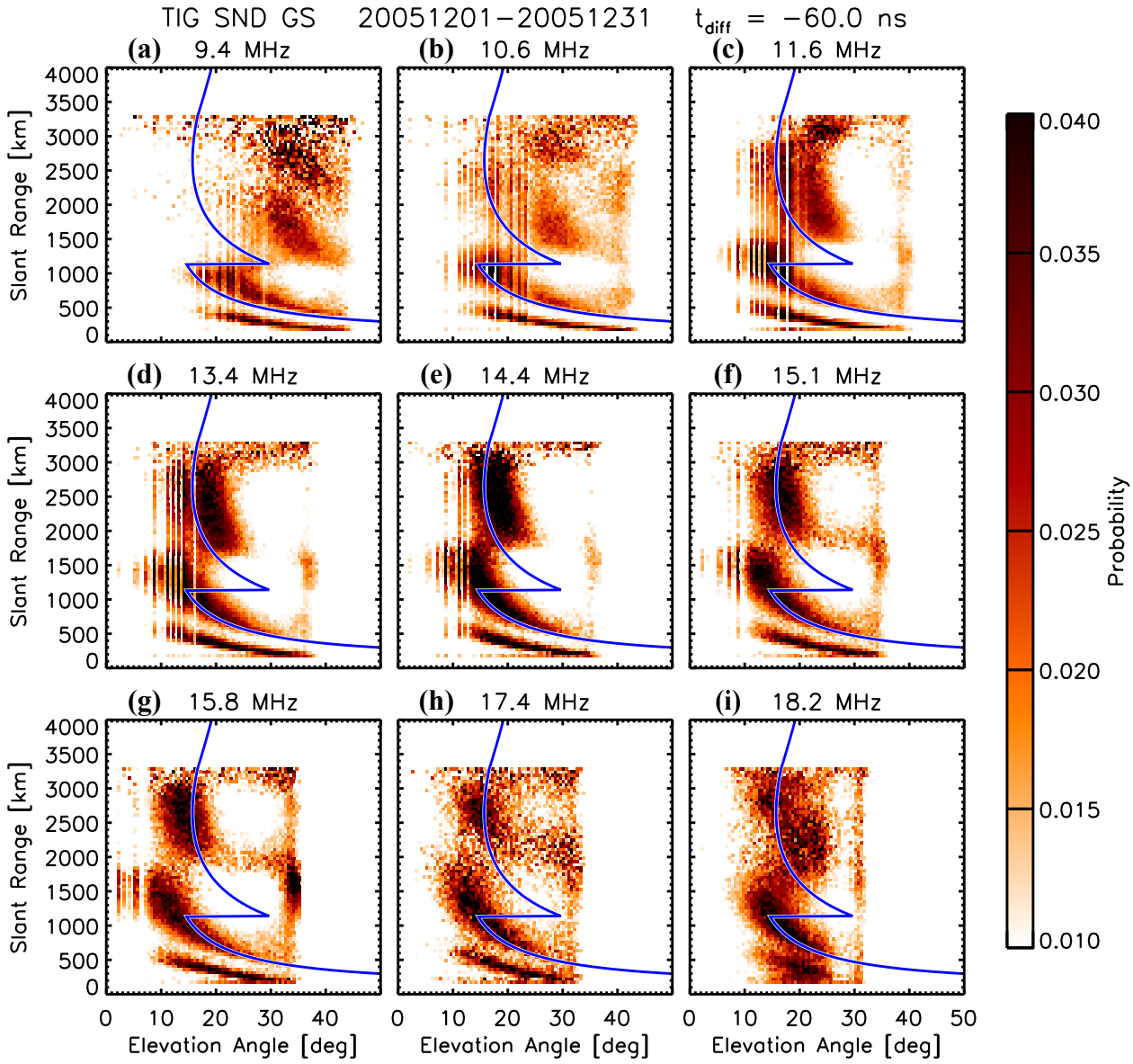

Figure 6. Joint probability distributions of elevation angle and slant range for ground scatter observed by the TIG radar during the entire month of Dec 2005 in the same format as Figure 5, using a revised $t_{\rm diff}$ value of −60 ns.

The TIG elevation-range distributions appear quite reasonable at frequencies above 14.4 MHz (Figures 5e–i). Below 14.4 MHz however, the majority of the data at each range are aliased to very large elevation angles, similar to the GBR results in Figure 3. Applying the multi-frequency calibration technique suggests a $t_{\rm diff}$ value of −60 ns, the result of which can be seen in Figure 6. The GS distributions at higher frequencies remain largely unchanged from those in Figure 5, while at lower frequencies they are now in much better agreement with the CV VHM. This result (or agreement) can be understood in terms of the inherent 2π measurement ambiguity of SuperDARN interferometry, as 60 ns corresponds to the period of a 16.7 MHz wave, which lies near the middle of the upper TIG sounding frequencies (14.4 MHz / 69.4 ns and 18.2 MHz / 54.9 ns). An equivalent

Table 1. t_{diff} values found by applying multi-frequency calibration to SuperDARN radars participating in 2023 sounding mode experiments.

Radar Name	Code	t_{diff} (ns)
Clyde River	CLY	0
Christmas Valley East	CVE	-398
Christmas Valley West	CVW	-346
Goose Bay	GBR	-63
Hokkaido East	HOK	-40
Iceland East	ICE	-300
Iceland West	ICW	-380
Inuvik	INV	0
Kapuskasing	KAP	-34
Prince George	PGR	14
Rankin Inlet	RKN	45
Saskatoon	SAS	5

set of figures showing the pre- and post-calibrated TIG sounding mode results for IS echoes are available in the supplementary material.

Beginning in April 2023, network-wide sounding mode experiments have been conducted for three consecutive days each month using an updated version of the radar control software originally developed by Hughes et al. (2002). The sounding mode data are now stored using the same format as the standard SuperDARN RawACF and FitACF files and can be processed using the open source Radar Software Toolkit (RST) (SuperDARN Data Analysis Working Group et al., 2022). The new data files also retain the observed phase differences (ψ_{obs}) for easier application of post-processing calibration techniques. Note the multi-frequency data from the ICW radar shown in section 2 were obtained using this new sounding mode. In Table 1, we provide t_{diff} estimates for each of the participating SuperDARN radars found by applying the multi-frequency calibration approach to the 2023 sounding mode data. We hope the values in Table 1 will not only aid researchers attempting to use elevation data from these radars but also for future validation against other interferometer calibration techniques.

5 Discussion

The multi-frequency calibration approach improves upon the original virtual height comparison method (Chisham et al., 2021) by resolving the 2π measurement ambiguity when estimating t_{diff}. However there remain several limitations to this technique which must be addressed. First, it requires radar measurements obtained at different operating frequencies which ideally span several MHz. Many SuperDARN radars operate in a fixed frequency band while others use separate frequency bands for daytime and nighttime operation to try to optimize the amount of observed backscatter. It is therefore not always possible to apply this technique to historical observations for resolving the 2π ambiguity in t_{diff} if a radar did not collect data at a range of different operating frequencies.

Another source of uncertainty is associated with the use of an empirical VHM against which to compare the elevation angles calculated for different values of t_{diff} at different radar operating frequencies. For example, the Chisham VHM was derived using 5 years of data from a single high-latitude radar (Saskatoon) during solar cycle 23, while the more recent CV VHM was derived using 5 years of data during solar cycle 24 from two mid-latitude radars. HF propagation conditions are known to vary based on local time, sea-

son, and solar cycle conditions; therefore, use of the Chisham or CV VHM may not be appropriate for all radars under all geophysical conditions. More fundamentally, this technique also assumes that t_{diff} was properly calibrated when deriving the VHM.

Thomas and Shepherd (2022) demonstrated that, in a climatological sense, HF propagation modes for backscatter from ionospheric irregularities are similar at both auroral and mid-latitudes. In the absence of more comprehensive empirical VHMs, which can describe a broader range of HF propagation conditions, we believe the CV VHM is currently best suited for this multi-frequency calibration technique as it allows for the inclusion of a significantly larger amount of input data as opposed to VHMs which only support ionospheric propagation modes. Improved performance could also be achieved by adjusting the ranges at which the VHMs change from one propagation mode to another as a function of frequency. This behavior can be clearly seen in Figure 6, where the transition between 1-hop E-region GS and 1-hop F-region GS varies from ∼1000 km at 9.4 MHz to ∼1700 km at 18.2 MHz, while the CV VHM transition remains fixed at 1140 km.

Of course, the underlying principle behind the multi-frequency calibration approach (i.e., to account for the 2π measurement ambiguity in the observed phase difference) does not require the use of an empirical VHM at all. This technique can be generalized to any of the other calibration techniques using meteor echoes or other IS or GS targets simply by comparing results at multiple (well-spaced) radar operating frequencies. Or, the multi-frequency method as described here could be applied first to provide a rough estimate of t_{diff} for all frequencies, which could then be further refined using another technique. We must also note that our approach assumes t_{diff} to be frequency independent, which has held true for all of the SuperDARN radars evaluated so far.

6 Summary

In this study we have presented a new approach for calibrating SuperDARN interferometer measurements which can be applied to even the earliest available data. Using both ionospheric and ground backscatter observations from a diverse set of radar operating frequencies, one can automatically identify the electrical path length difference (t_{diff}) which best agrees with empirical HF propagation characteristics at all frequencies. We have successfully applied this technique to obtain t_{diff} estimates for a dozen radars using multi-frequency observations from the past year. By regularly conducting multi-frequency sounding campaigns, this technique can allow for continuous calibration of elevation angles and therefore improved geolocation of all SuperDARN backscatter observations.

7 Open Research

The raw SuperDARN data used in this study are available from the British Antarctic Survey SuperDARN data mirror (https://www.bas.ac.uk/project/superdarn/#data). While data for this study were accessed from the British Antarctic Survey, they may also be obtained from the Canadian Federated Research Data Repository (FRDR) at https://www.frdr-dfdr.ca/repo/collection/superdarn. The Radar Software Toolkit to read and process the SuperDARN data can be downloaded from Zenodo (SuperDARN Data Analysis Working Group et al., 2022).

Acknowledgments
This research was funded by the Office of Naval Research under grant N000142312109, by the Air Force Research Laboratory under grant FA94532220027, and by the National Science Foundation under grants OPP-1836426 and AGS-1934997. The authors acknowledge the use of SuperDARN data. SuperDARN is a collection of radars funded by the

national scientific funding agencies of Australia, Canada, China, France, Italy, Japan, Norway, South Africa, United Kingdom, and the United States of America. Operation of the Iceland West and Goose Bay radars is supported by the National Science Foundation. The authors acknowledge the use of data provided by the TIGER Consortium Partners and their supporting funding organizations: Australian Research Council and US AFOSR.

References

André, D., Sofko, G. J., Baker, K., & MacDougall, J. (1998). SuperDARN interferometry: Meteor echoes and electron densities from groundscatter. *J. Geophys. Res.*, *103*(A4), 7003–7015. doi: 10.1029/97JA02923

Bristow, W. A., Lyons, L. R., Nishimura, Y., Shepherd, S. G., & Donovan, E. F. (2022). High-latitude plasma convection based on SuperDARN observations and the locally divergence free criterion. *J. Geophys. Res. Space Physics*, *127*, e2022JA030883. doi: 10.1029/2022JA030883

Burrell, A. G., Yeoman, T. K., Milan, S. E., & Lester, M. (2016). Phase calibration of interferometer arrays at high-frequency radars. *Radio Sci.*, *51*, 1445–1456. doi: 10.1002/2016RS006089

Chisham, G. (2018). Calibrating SuperDARN interferometers using meteor backscatter. *Radio Sci.*, *53*, 761–774. doi: 10.1029/2017RS006492

Chisham, G., Burrell, A. G., Marchaudon, A., Shepherd, S. G., Thomas, E. G., & Ponomarenko, P. (2021). Comparison of interferometer calibration techniques for improved SuperDARN elevation angles. *Polar Sci.*, *28*, 100638. doi: 10.1016/j.polar.2021.100638

Chisham, G., & Freeman, M. P. (2013). A reassessment of SuperDARN meteor echoes from the upper mesosphere and lower thermosphere. *J. Atmos. Sol.-Terr. Phys.*, *102*, 207–221. doi: 10.1016/j.jastp.2013.05.018

Chisham, G., Lester, M., Milan, S. E., Freeman, M. P., Bristow, W. A., Grocott, A., ... Walker, A. D. M. (2007). A decade of the Super Dual Auroral Radar Network (SuperDARN): Scientific achievements, new techniques and future directions. *Surv. Geophys.*, *28*(1), 33–109. doi: 10.1007/s10712-007-9017-8

Chisham, G., Yeoman, T. K., & Sofko, G. J. (2008). Mapping ionospheric backscatter measured by the SuperDARN HF radars – Part 1: A new empirical virtual height model. *Ann. Geophys.*, *26*, 823–841. doi: 10.5194/angeo-26-823-2008

Greenwald, R. A., Baker, K. B., Dudeney, J. R., Pinnock, M., Jones, T. B., Thomas, E. C., ... Yamagishi, H. (1995). DARN/SuperDARN: A global view of the dynamics of high-latitude convection. *Space Sci. Rev.*, *71*(1), 761–796. doi: 10.1007/BF00751350

Greenwald, R. A., Frissell, N., & de Larquier, S. (2017). The importance of elevation angle measurements in HF radar investigations of the ionosphere. *Radio Sci.*, *52*, 305–320. doi: 10.1002/2016RS006186

Hughes, J. M., Bristow, W. A., & Greenwald, R. A. (2002). Determining characteristics of HF communications links using SuperDARN. *Ann. Geophys.*, *20*, 1023–1030. doi: 10.5194/angeo-20-1023-2002

Milan, S. E., Jones, T. B., Robinson, T. R., Thomas, E. C., & Yeoman, T. K. (1997). Interferometric evidence for the observation of ground backscatter originating behind the CUTLASS coherent HF radars. *Ann. Geophys.*, *15*, 29–39. doi: 10.1007/s00585-997-0029-y

Nishitani, N., Ruohoniemi, J. M., Lester, M., Baker, J. B. H., Koustov, A. V., Shepherd, S. G., ... Kikuchi, T. (2019). Review of the accomplishments of mid-latitude Super Dual Auroral Radar Network (SuperDARN) HF radars. *Prog Earth Planet Sci*, *6:27*. doi: 10.1186/s40645-019-0270-5

Ponomarenko, P. V., Nishitani, N., Oinats, A. V., Tsuya, T., & St. Maurice, J.-P. (2015). Application of ground scatter returns for calibration of HF interferom-

etry data. *Earth Planet Sp*, *67:138*. doi: 10.1186/s40623-015-0310-3

Ponomarenko, P. V., St. Maurice, J.-P., & McWilliams, K. A. (2018). Calibrating HF radar elevation angle measurements using *E* layer backscatter echoes. *Radio Sci.*, *53*, 1438–1449. doi: 10.1002/2018RS006638

Ruohoniemi, J. M., & Baker, K. B. (1998). Large-scale imaging of high-latitude convection with Super Dual Auroral Radar Network HF radar observations. *J. Geophys. Res.*, *103*(A9), 20797–20811. doi: 10.1029/98JA01288

Shepherd, S. G. (2017). Elevation angle determination for SuperDARN HF radar layouts. *Radio Sci.*, *52*, 938–950. doi: 10.1002/2017RS006348

SuperDARN Data Analysis Working Group, Thomas, E. G., Reimer, A. S., Bland, E. C., Burrell, A. G., Grocott, A., ... Walach, M.-T. (2022). *SuperDARN Radar Software Toolkit (RST) 5.0* [Software]. Zenodo. doi: 10.5281/zenodo.7467337

Thomas, E. G., & Shepherd, S. G. (2022). Virtual height characteristics of ionospheric and ground scatter observed by mid-latitude SuperDARN HF radars. *Radio Sci.*, *57*, e2022RS007429. doi: 10.1029/2022RS007429

Figure 1.

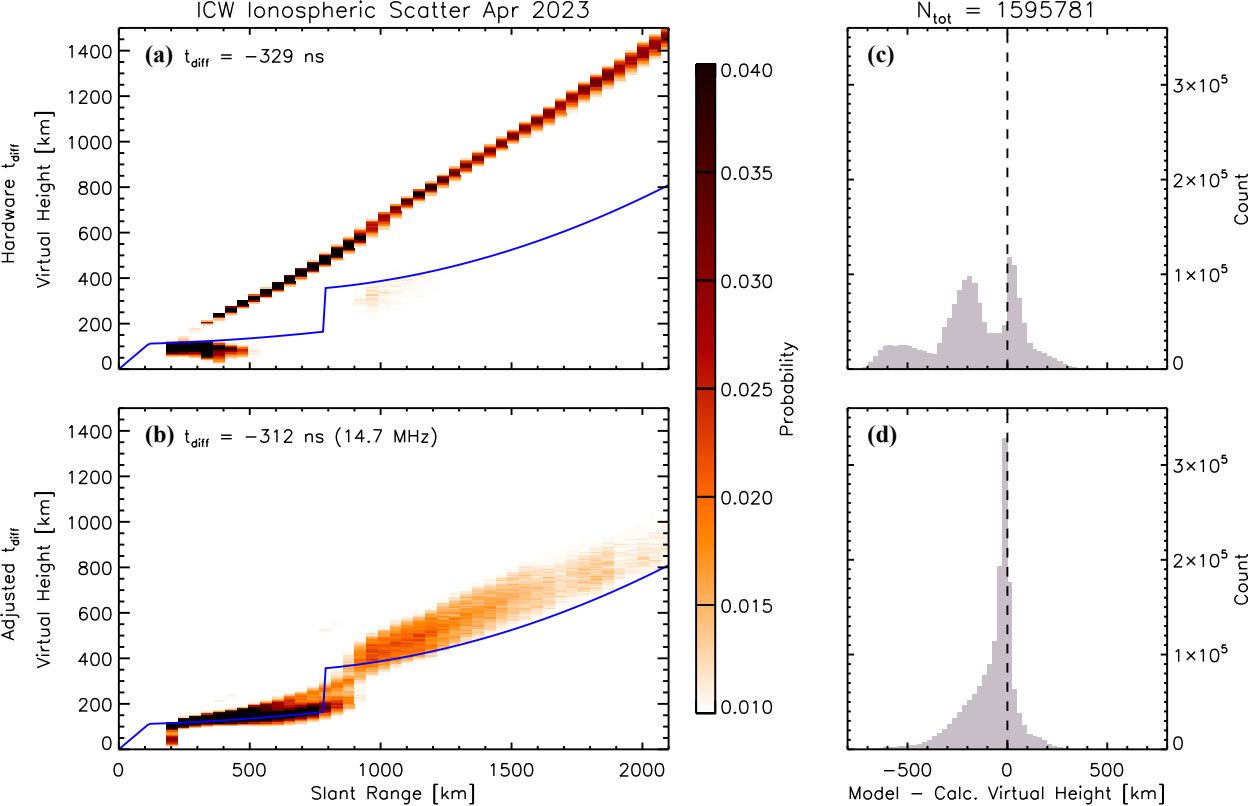
ICW Ionospheric Scatter Apr 2023
N_tot = 1595781
(a) t_diff = −329 ns
(b) t_diff = −312 ns (14.7 MHz)
(c)
(d)
Hardware t_diff
Adjusted t_diff
Virtual Height [km]
Slant Range [km]
Probability
Count
Model − Calc. Virtual Height [km]

Figure 2.

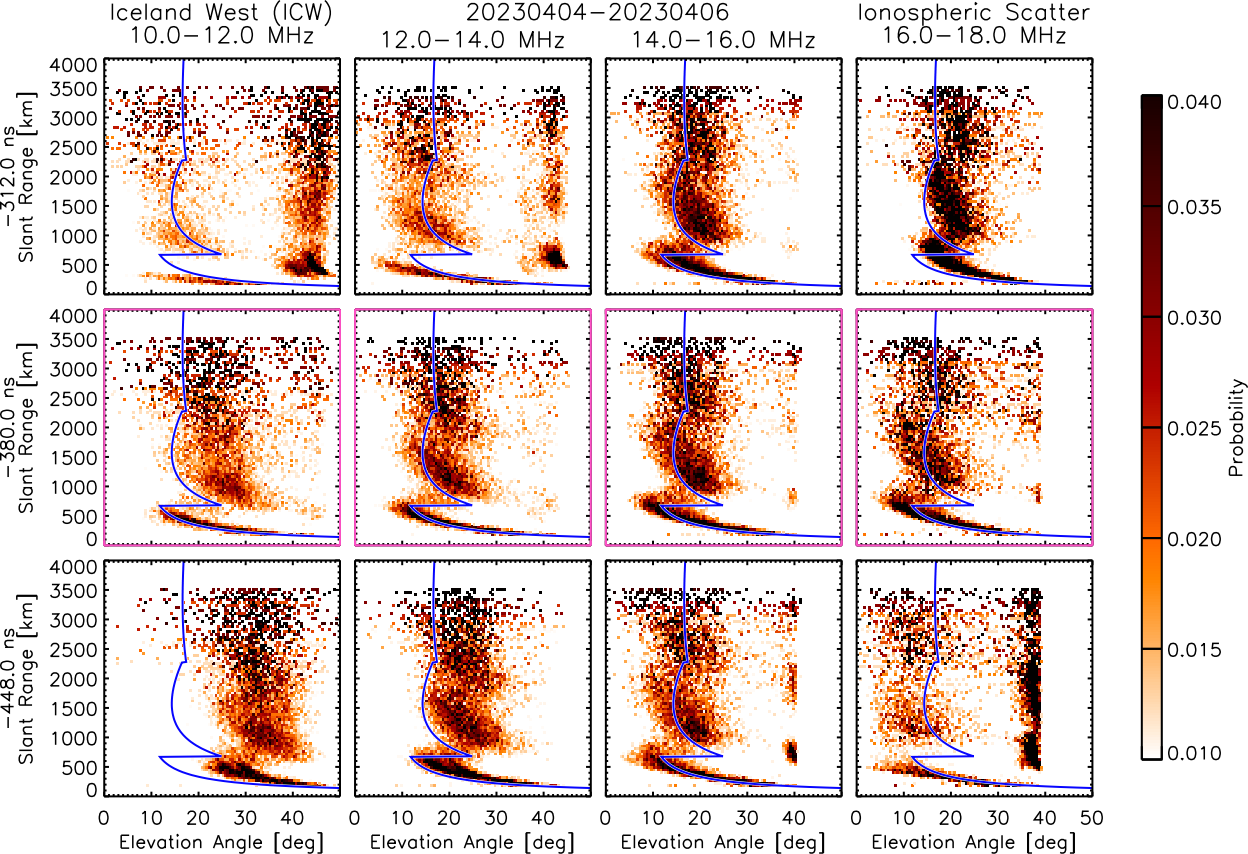
Iceland West (ICW)
10.0–12.0 MHz
20230404–20230406
12.0–14.0 MHz
14.0–16.0 MHz
Ionospheric Scatter
16.0–18.0 MHz
−312.0 ns
−380.0 ns
−448.0 ns
Slant Range [km]
Elevation Angle [deg]
Probability
0.040
0.035
0.030
0.025
0.020
0.015
0.010

Figure 3.

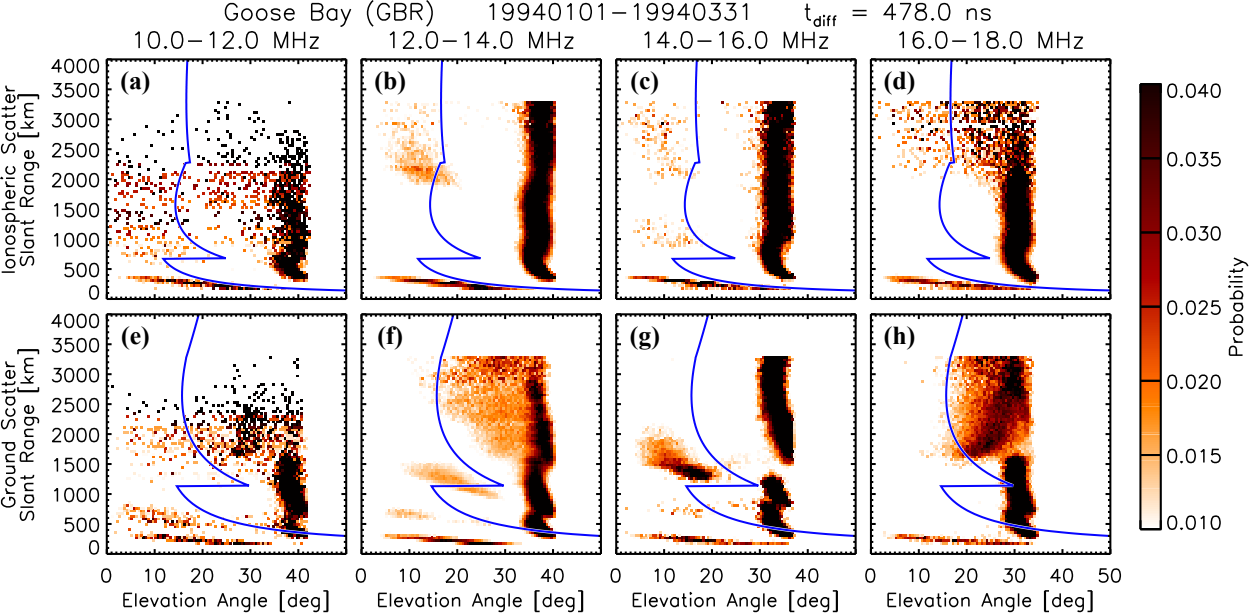
Goose Bay (GBR) 19940101–19940331 t_{diff} = 478.0 ns
10.0–12.0 MHz
12.0–14.0 MHz
14.0–16.0 MHz
16.0–18.0 MHz
(a)
(b)
(c)
(d)
(e)
(f)
(g)
(h)
Ionospheric Scatter Slant Range [km]
Ground Scatter Slant Range [km]
0
500
1000
1500
2000
2500
3000
3500
4000
0
10
20
30
40
50
Elevation Angle [deg]
Probability
0.010
0.015
0.020
0.025
0.030
0.035
0.040

Figure 4.

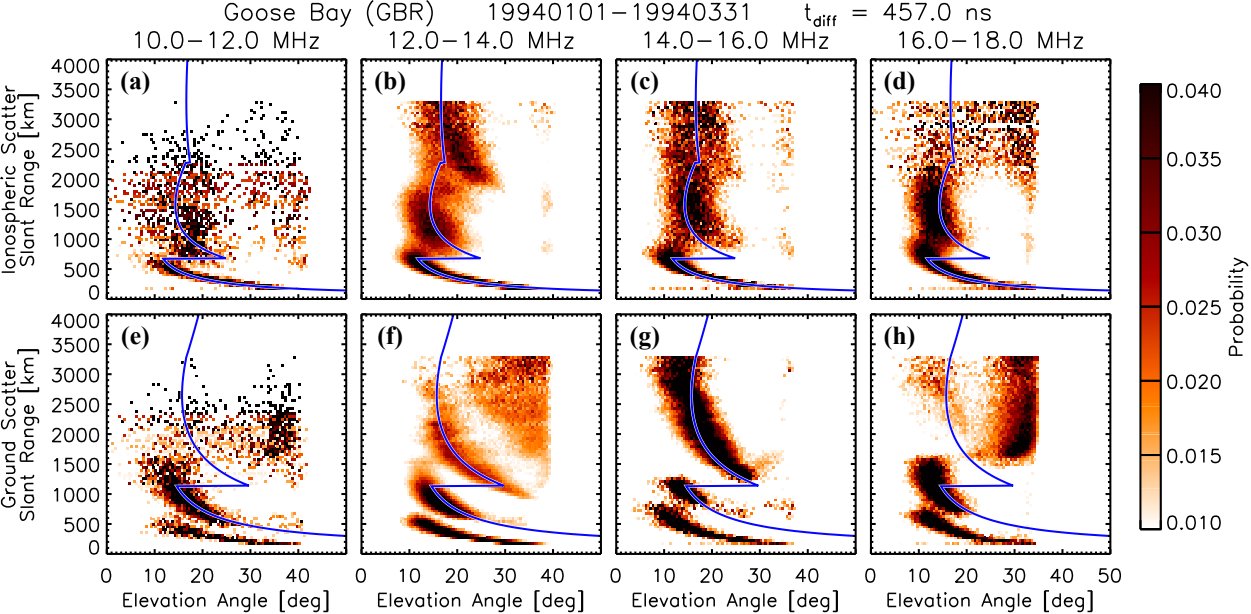
Goose Bay (GBR) 19940101–19940331 t_{diff} = 457.0 ns
10.0–12.0 MHz
12.0–14.0 MHz
14.0–16.0 MHz
16.0–18.0 MHz
(a)
(b)
(c)
(d)
(e)
(f)
(g)
(h)
Ionospheric Scatter Slant Range [km]
Ground Scatter Slant Range [km]
0
500
1000
1500
2000
2500
3000
3500
4000
0
10
20
30
40
50
Elevation Angle [deg]
Probability
0.010
0.015
0.020
0.025
0.030
0.035
0.040

Figure 5.

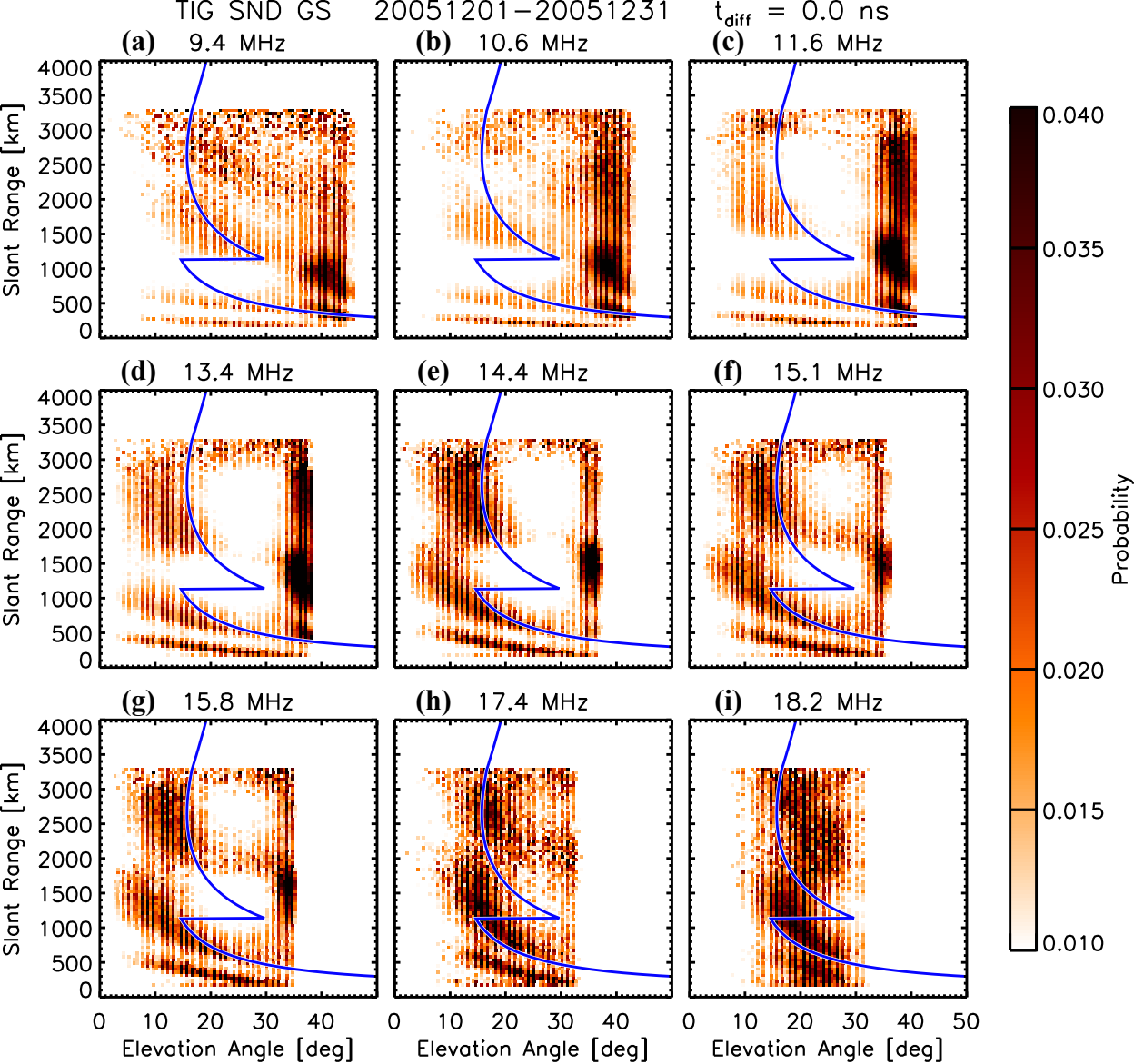
TIG SND GS 20051201–20051231 t_{diff} = 0.0 ns
(a) 9.4 MHz
(b) 10.6 MHz
(c) 11.6 MHz
(d) 13.4 MHz
(e) 14.4 MHz
(f) 15.1 MHz
(g) 15.8 MHz
(h) 17.4 MHz
(i) 18.2 MHz
Slant Range [km]
0
500
1000
1500
2000
2500
3000
3500
4000
Elevation Angle [deg]
0
10
20
30
40
50
Probability
0.010
0.015
0.020
0.025
0.030
0.035
0.040

Figure 6.

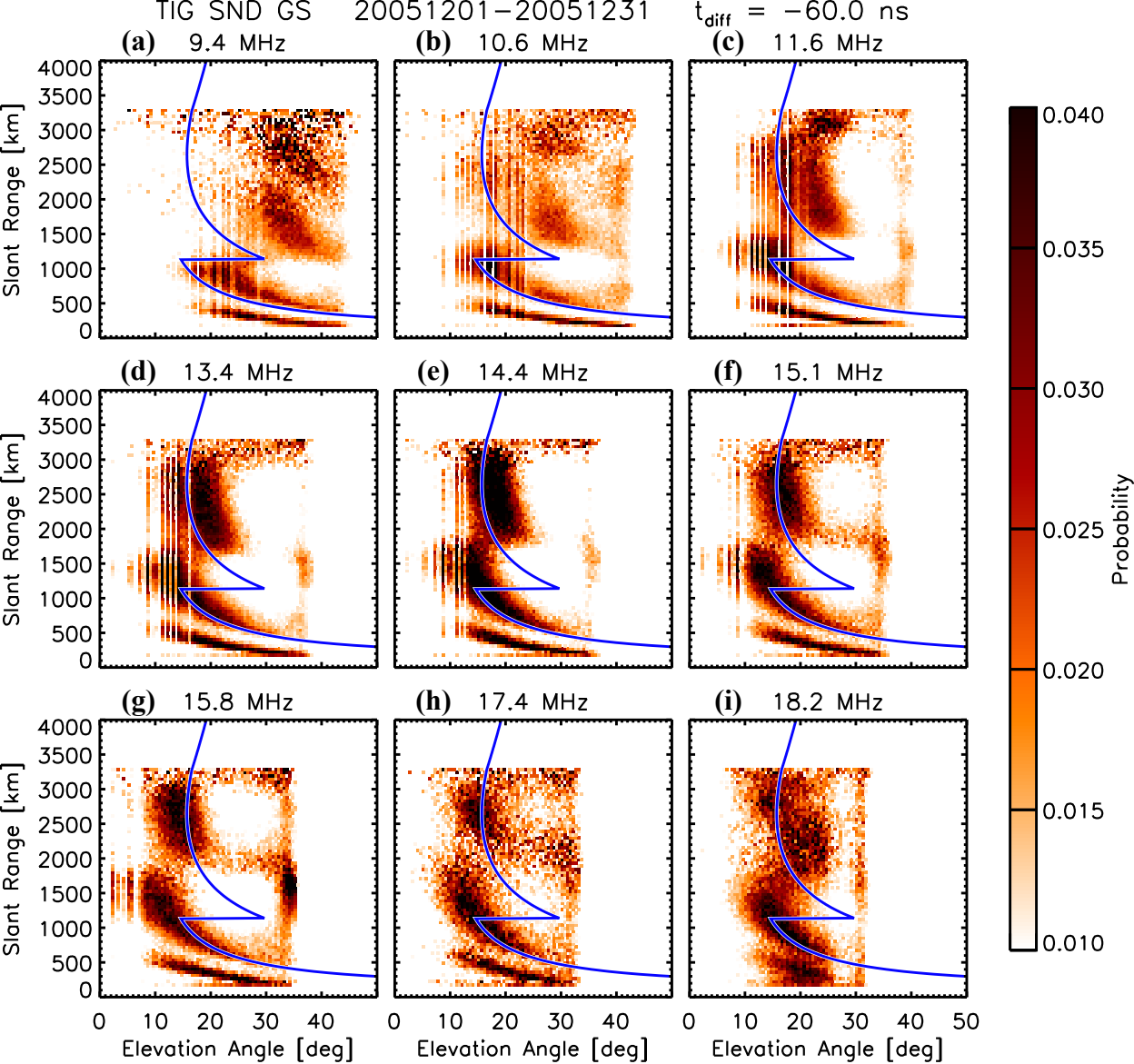
TIG SND GS 20051201–20051231 t_{diff} = −60.0 ns
(a) 9.4 MHz
(b) 10.6 MHz
(c) 11.6 MHz
(d) 13.4 MHz
(e) 14.4 MHz
(f) 15.1 MHz
(g) 15.8 MHz
(h) 17.4 MHz
(i) 18.2 MHz
Slant Range [km]
0
500
1000
1500
2000
2500
3000
3500
4000
0
10
20
30
40
50
Elevation Angle [deg]
Probability
0.010
0.015
0.020
0.025
0.030
0.035
0.040